# Identifying the non-exceedance probability of extreme storm surges as a component of natural-disaster management using tidal-gauge data from Typhoon Maemi in South Korea

5   Sang-Guk Yum[1], Hsi-Hsien Wei[2], Sung-Hwan Jang[3,4]

[1]Department of Civil Engineering and Engineering Mechanics, Columbia University, New York, NY 10027, USA; sy2509@columbia.edu
[2]Department of Building and Real Estate, The Hong Kong Polytechnic University, Kwoloon, Hong Kong, PR China;
10   hhwei@polyu.edu.hk, hhweing@gmail.com
[3]Department of Civil and Environmental Engineering, Hanyang University ERICA, Ansan, Gyeonggi-do 15588, South Korea; sj2527@hanyang.ac.kr
[4]Department of Smart City Engineering, Hanyang University ERICA, Ansan, Gyeonggi-do 15588, South Korea; sj2527@hanyang.ac.kr

*Correspondence to*: Sung-Hwang Jang (sj2527@hanyang.ac.kr)

**Abstract.** Global warming, one of the most serious aspects of climate change, can be expected to cause rising sea levels. These, in turn, have been linked to unprecedentedly large typhoons that can cause flooding of low-lying land, coastal invasion, seawater flows into rivers and groundwater, rising river levels, and aberrant tides. To prevent loss of life and
20   property damage caused by typhoons, it is crucial to accurately estimate storm surge related risk. This study therefore develops a statistical model for estimating probability model, based on surge data pertaining to Typhoon Maemi, which struck South Korea in 2003. Specifically, estimation of non-exceedance probability models of the typhoon-related storm surge was achieved via clustered separated peaks-over-threshold simulation, while various distribution models were fitted to the empirical data for investigating the risk of storm surge height. The result of this process found that the result of Weibull
25   distribution was better than other distribution model for Typhoon Maemi's peak total water level.

## 1 Introduction

### 1.1 Climate change and global warming

Climate change, which can directly affect the atmosphere, oceans, icebergs, and other planetary features via a variety of pathways and mechanisms, notably including global warming, also has secondary consequences for nature and for human
30   society. In the specific case of global warming, one of the most profoundly negative of these secondary effects consists of

sea-level rises, which can cause flooding of low-lying land, coastal invasion, seawater flows into rivers and groundwater, river-level rises, and tidal aberrations.

Recent research has also reported that, under the influence of global warming, the intensities and frequencies of typhoons and hurricanes are continuously changing, increasing these hazards' potential to negatively affect water resources, transportation facilities, and other infrastructure, as well as natural systems (Noshadravan et al. 2017). In such circumstances, the protection of human society calls for highly accurate forecasting systems, especially as inaccurate estimation of the risk probability of these hazards can lead to the construction of facilities in inappropriate locations, thus wasting time and money as well as endangering life. Moreover, the combined effect of sea-level rises and tropical storms is potentially even more catastrophic than either of these hazards by itself.

### 1.1.1 Sea-level rises

According to the Intergovernmental Panel on Climate Change (IPCC, 2007), average global temperature increased by approximately 0.74℃ (i.e., at least 0.56℃ and up to 0.92℃) between 1906 and 2005 (Hwang and Deodatis 2013). The IPCC's (2007) Fourth Assessment Report (AR4) noted that since 1961, world mean sea level (MSL) has increased by around 1.8mm (i.e., 1.3-2.3mm) per year; and when melting icebergs are taken into account, this figure increases to 3.1mm (2.4-3.8mm). Moreover, the overall area of Arctic ice has decreased by an average of 2.7% annually since 1978, and the amount of snow on mountains has also declined (Kim and Cho 2013). These observations have sparked growing interest in how much sea levels will increase, including research on how changes in the climate can best be coped with (Radic and Hock 2011; Schaeffer et al. 2012). Most industrial facilities on the Korean Peninsula, including plants, ports, roads, and shipyards, are located near the shore – as, indeed, are most residential buildings. Those topographical characteristics make the cities of South Korea especially vulnerable to damage caused by sea-level rises and the associated large socioeconomic losses.

### 1.1.2 Sea-level rises potentially affecting the city of Busan, South Korea

Yoon and Kim (2012) investigated 51 years' worth of sea-level changes using data from tidal gauges at 17 stations located around the Korean Peninsula. They utilized regression analysis to calculate the general trend in MSL for 1960-2010 at each station, and found that around Korea, MSL rose more quickly than it did globally. The linear rising trend of MSL was relatively small along Korea's western coast (averaging 1.3mm/year), but large on the southern and eastern coasts (3.2mm/year and 2.0mm/year, respectively), and very large around Jeju Island (5.6mm/year, i.e., more than three times the global average).

According to AR4, the rate of sea-level rises may accelerate after the 21st century, and this should be taken into consideration when designing coastal structures if disasters are to be avoided. Therefore, places most likely to be affected by current and future climate change need more accurate predictions of sea-level variation and surge heights, surge being

defined as the difference between observed and predicted sea level. In the present study, Busan, a major metropolitan area on
the south-eastern coast of South Korea, has been used as a case study. According to Yoon and Kim's (2012) calculations, the
65   sea level around Busan rose by an average 1.8mm/year from 1960 to 2010, i.e., roughly the same as the global trend over the
same period.

## 1.2 Problem statement

### 1.2.1 Typhoon trends in South Korea

70   The Korean Peninsula is bounded by three distinct sea-systems, generally known in English as the Yellow Sea, the Korea
Strait, and the Sea of Japan. This characteristic has often led to severe damage to its coastal regions. According to the Korea
Ocean Observing and Forecasting System (KOOFS), Typhoon Maemi in September 2003 had a maximum wind speed of 54
meters per second (m/s), and caused US$35 billion in property damage, as shown in Table 1. All three of the highest peaks
ever recorded by South Korea's tidal-gauge stations also occurred in that month.

75                             Table 1. Largest typhoons to have struck the Korean Peninsula

| Name | Date | Amount of Damage (US$) | Max. Wind Speed (10 min. avg., m/s) |
|---|---|---|---|
| Rusa | Aug. 30-Sep. 1, 2002 | 4.3 billion (1st) | 41 |
| Maemi | Sep. 12-13, 2003 | 3.5 billion (2nd) | 54 |
| Bolaven | Aug. 25-30, 2012 | 0.9 billion (3rd) | 53 |

The most typhoon-heavy month there is August, followed by July and September, with two-thirds of all typhoons occurring
in July and August. Tables 2 and 3, below, present statistics about typhoons in South Korea over periods of 68 years and
recent 10 years, respectively; Figure 1 shows the track of Typhoon Maemi from September 4 to September 16, 2003. As can
80   be seen from Figures 1, Typhoon Maemi passed into Busan from the southeast, causing direct damage upon landfall, after
which its maximum 10-minute sustained wind speed was 54 m/s. Typhoon Maemi prompted the insurance industry, the
Korean government, and many academic researchers to recognize the importance of advance planning and preparations for
such storms, as well as for other types of natural disasters.

Table 2. Incidence of typhoons and typhoon landfall in South Korea, 1952 - 2019, by month

| | Jan. | Feb. | Mar. | Apr. | May | Jun. | Jul. | Aug. | Sep. | Oct. | Nov. | Dec. | |
|---|---|---|---|---|---|---|---|---|---|---|---|---|---|
| Sum | 29 | 15 | 15 | 45 | 67 | 115 | 245 | 351 | 322 | 238 | 152 | 73 | 1,678 |
| Average | 0.54 | 0.28 | 0.46 | 0.83 | 1.24 | 2.13 | 4.54 | 6.52 | 5.96 | 4.41 | 2.81 | 1.35 | 31.07 |
| Landfall (sum) | 0 | 0 | 0 | 0 | 1 | 18 | 65 | 70 | 45 | 5 | 0 | 0 | 206 |

| | | | | | | | | | | | | |
|---|---|---|---|---|---|---|---|---|---|---|---|---|
| Landfall (average) | 0.0 | 0.0 | 0.0 | 0.0 | 0.02 | 0.33 | 1.2 | 1.3 | 0.87 | 0.09 | 0.0 | 0.0 | 3.81 |

85

Table 3. Incidence of typhoons and typhoon landfall in South Korea, 2010 - 2019, by month

| | Jan. | Feb. | Mar. | Apr. | May | Jun. | Jul. | Aug. | Sep. | Oct. | Nov. | Dec. | |
|---|---|---|---|---|---|---|---|---|---|---|---|---|---|
| Sum | 4 | 3 | 4 | 5 | 12 | 18 | 33 | 43 | 56 | 34 | 16 | 7 | 235 |
| Average | 0.4 | 0.3 | 0.4 | 0.5 | 1.2 | 1.8 | 3.3 | 4.3 | 5.6 | 3.4 | 1.6 | 0.7 | 23.5 |
| Landfall (sum) | 0 | 0 | 0 | 0 | 0 | 0 | 3 | 11 | 7 | 5 | 2 | 0 | 28 |
| Landfall (average) | 0 | 0 | 0 | 0 | 0 | 0 | 0.3 | 1.1 | 0.7 | 0.5 | 0.2 | 0 | 2.8 |

Figure 1. Track and wind speed of Maemi, 2003

90   Figure 1 was based on data collected by Korea Hydrographic and Oceanographic Agency and created by authors using

ArcGIS software product

### 1.2.2 Tidal gauge stations in South Korea

Effective measures for reducing the damage caused by future typhoons, including especially the design and re-design of

waterfront infrastructure, will require accurate prediction of storm-surge height. As of 2019, South Korea operated 17 tidal-

95   gauge stations, of which eight had been collecting data for 30 years or more. They were located on the western (n=5),

southern (n=10), and eastern coasts (n=2).
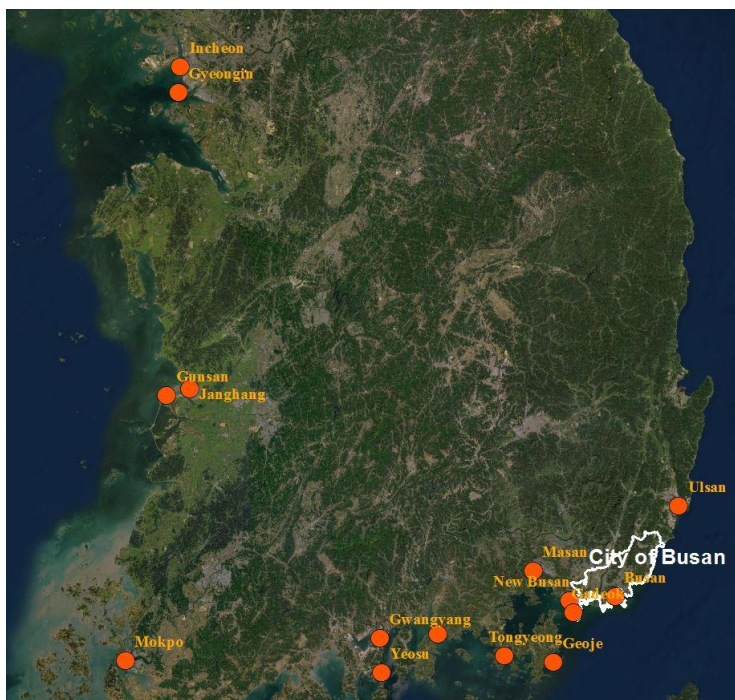
Figure 2. Locations of tidal-gauge stations on the western and southern coasts of South Korea

Figure 2 was based on data collected by Korea Hydrographic and Oceanographic Agency and created by authors using

100   ArcGIS software product

This study focuses on the 15 tidal-gauge stations located on the southern and western coasts (Figure 2). The reason for

excluding the remaining two stations is that the majority of typhoons do not arrive from the east or make landfall on that

coast. The hourly tidal data for this study has been provided by the Korea Hydrographic and Oceanographic Agency (KHOA)

105   and is used with that agency's permission.

### 1.2.3 Highest recorded water levels

The western tidal-gauge stations are located at Incheon, Gyeongin, Changwon, Gunsan, and Mokpo. Each of the five has operated for a different length of time, ranging from 2 to 61 years. After collecting the sea levels observed hourly by each station throughout their respective periods of operation, the top three sea-level heights at each were obtained. These heights, which are shown in Table 4, are clearly correlated with the dates of arrival of typhoons.

Table 4. Three highest water levels recorded at each tidal-gauge station on Korea's west coast

| Location | Years of data | Top three peaks (cm) | Dates/times of peaks |
|---|---|---|---|
| Incheon | 18 | 987 | Jul. 24, 2013, 10:00 |
| | | 981 | Sep. 8, 2002, 06:00 |
| | | 980 | Oct. 27, 2003, 18:00 |
| Gyeonin | 2 | 993 | Sep. 30, 2015, 19:00 |
| | | 987 | Sep. 29, 2015, 18:00 |
| | | 986 | Oct. 29, 2015, 18:00 |
| Janghang | 14 | 798 | Sep. 30, 2015, 17:00 |
| | | 796 | Oct. 11, 2014, 17:00 |
| | | 794 | Sep. 29, 2015, 16:00 |
| Gunsan | 37 | 805 | Aug. 19, 1997, 04:00 |
| | | 799 | Aug. 21, 1997, 05:00 |
| | | 797 | Aug. 31, 2000, 05:00 |
| Mokpo | 61 | 544 | Jul. 4, 2004, 04:00 |
| | | 544 | Jul. 6, 2004, 05:00 |
| | | 538 | Nov. 16, 2012, 16:00 |

The same approach was applied to the data from the 10 tidal-gauge stations on the south coast, as shown in Tables 5 and 6, below.

Table 5. Three highest water levels recorded at each tidal-gauge station on Korea's south coast

| Location | Years of data | Top three peaks (cm) | Dates/times of peaks |
|---|---|---|---|
| New Busan | 5 | 221 | Sep. 18, 2012, 10:00 |
| | | 219 | Sep. 17, 2012, 09:00 |
| | | 219 | Aug. 11, 2014, 21:00 |
| Gadeok | 40 | 252 | Sep. 17, 2012, 10:00 |
| | | 246 | Sep. 17, 2012, 09:00 |
| | | 246 | Jul. 16, 1987, 00:00 |
| Masan | 37 | 265 | Sep. 17, 2012, 10:00 |

| | | 264 | Sep. 17, 2012, 11:00 |
| | | 244 | Aug. 29, 2004, 21:00 |
| Ulsan | 55 | 133 | Aug. 19, 2004, 08:00 |
| | | 120 | Sep. 12, 2003, 21:00 |
| | | 129 | Sep. 17, 2012, 20:00 |
| Tongyeong | 41 | 426 | Sep. 12, 2003, 21:00 |
| | | 357 | Sep. 12, 2012, 10:00 |
| | | 356 | Sep. 12, 2003, 20:00 |
| Samcheonpo | 2 | 352 | Aug. 30, 2015, 22:00 |
| | | 350 | Oct. 28, 2015, 09:00 |
| | | 350 | Nov. 27, 2015, 10:00 |
| Geoje | 11 | 270 | Sep. 17, 2012, 09:00 |
| | | 259 | Sep. 17, 2012, 10:00 |
| | | 255 | Jan. 4, 2006, 09:00 |
| Gwangyang | 6 | 479 | Sep. 17, 2012, 10:00 |
| | | 443 | Sep. 17, 2012, 11:00 |
| | | 441 | Aug. 1, 2014, 22:00 |
| Yeosu | 52 | 440 | Aug. 18, 1966, 23:00 |
| | | 430 | Sep. 14, 1966, 21:00 |
| | | 129 | Aug. 17, 1966, 22:00 |

115

### 1.2.4 Tidal gauge station at the City of Busan in South Korea

One of the focal tidal-gauge stations has observation records covering more than half a century. It is located on the south coast in Busan, South Korea's second-largest city. Thanks to its location near sea, Busan's international trade has boomed, and as a consequence it now boasts the largest port in South Korea. The Nakdong, longest and widest river in South Korea,

120 also passes through it. Due to these geographical characteristics, Busan has been very vulnerable to natural disasters, and the importance of accurately predicting the characteristics of future storms is increasingly recognized by its government and other stakeholders. The top three sea-level heights at the tidal-gauge station there are shown in Table 6, below.

Table 6. Three highest water levels recorded at the tidal gauge station in Busan, South Korea

| Busan | Years of data | Top three peaks (cm) | Dates/times of peaks |
|---|---|---|---|
| | 54 | 211 | Sep. 12, 2003, 21:00 |

| | | 190 | Sep. 12, 2003, 20:00 |
|---|---|---|---|
| | | 188 | Sep. 12, 2003, 12:00 |

Figures 4 and 5 show the annual MSL and fluctuations around the mean during the period 1956-2019 at Busan's tidal-gauge
station.
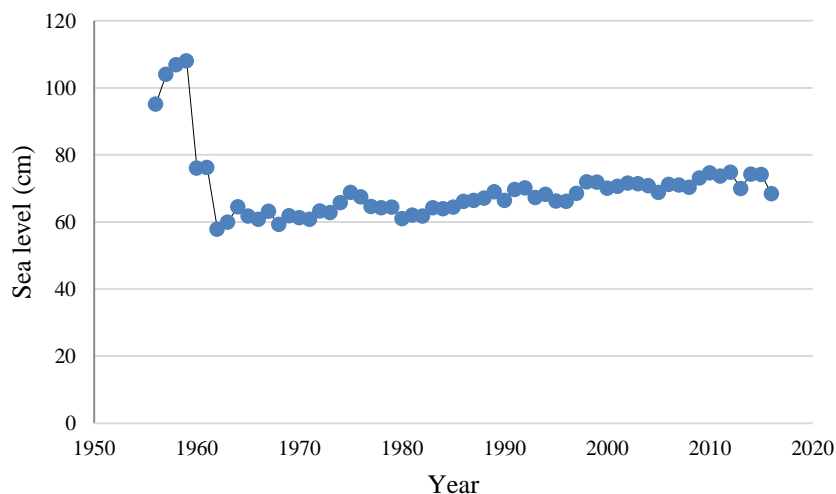
Figure 3. Sea-level history at Busan, South Korea, 1956-2019,

Korea Hydrographic and Oceanographic Agency

$y = 0.24x - 443.96$
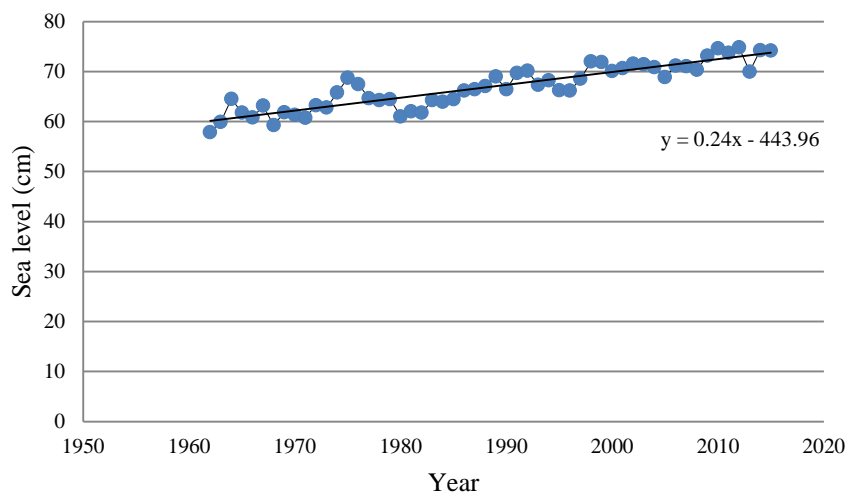
Figure 4. Sea-level fluctuations around the mean, Busan, South Korea, 1962-2019,

Korea Hydrographic and Oceanographic Agency

Looking at the sea-level history in Figure 3, it is clear that the data trend between 1956 and 1961 is anomalous. As this may have been due to quality-control issues with the observations from that period, it has been excluded from this study, and only data from 1962 to 2019 have been used, as shown in Figure 4. KHOA makes hourly observations of water height at the Busan tidal-gauge station, and our annual means have been calculated from this hourly data. As seen in Figure 4, plotting MSL for each year confirms that short-term water-level variation merely masks the long-term trend of sea-level increase. Therefore, acting on the assumption that MSL variation is a function of time, a linear regression was performed, with the resulting coefficient of slope indicating the rate of increase (Yoon and Kim 2012), i.e., y=0.24x-443.96 in our case.

From the above equation, it can be seen that the rate of increase in MSL at Busan's tidal-gauge station during 1962-2019 was 2.4mm per year, yielding a difference of 16.31cm between the end of that period and the beginning. This finding is broadly in line with Yoon and Kim's (2012), that the rate of MSL increase around the Korean Peninsula as a whole between 1960 and 2010 was about 2.9mm/year.

### 1.2.5 Relationship between sea level and typhoons

When a storm occurs, surge height tends to increase, and these larger surges can cause natural disasters such as floods. In this study, before calculating the height of a surge, we took account of the dates and times when the three greatest sea-level heights were observed, as well the dates and times when typhoons occurred. These data are presented side by side in Table 7.

Table 7. Relation between sea levels and typhoons on the south coast of Korea

| Location | Years | Peak (cm) | Date | Typhoon |
|---|---|---|---|---|
| Busan | 54 | 211 | Sep. 12, 2003, 21:00 | Maemi |
| | | 190 | Sep. 12, 2003, 20:00 | Maemi |
| | | 188 | Sep. 12, 2003, 12:00 | Maemi |
| New Busan | 5 | 221 | Sep. 18, 2012, 10:00 | Sanba |
| | | 219 | Sep. 17, 2012, 09:00 | Sanba |
| | | 215 | Sep. 18, 2012, 22:00 | Sanba |
| Gadeok | 40 | 252 | Sep. 17, 2012, 10:00 | Sanba |
| | | 246 | Sep. 17, 2012, 09:00 | Sanba |
| | | 246 | Jul. 16, 1987, 00:00 | Thelma |
| Masan | 37 | 265 | Sep. 17, 2012, 10:00 | Sanba |
| | | 264 | Sep. 17, 2012, 11:00 | n/a |
| | | 244 | Aug. 29, 2004, 21:00 | n/a |
| Ulsan | 55 | 133 | Aug. 19, 2004, 08:00 | Megi |

| | | 120 | Sep. 12, 2003, 21:00 | Maemi |
|---|---|---|---|---|
| | | 129 | Sep. 17, 2012, 20:00 | Sanba |
| Tongyeong | 41 | 426 | Sep. 12, 2003, 21:00 | Maemi |
| | | 357 | Sep. 12, 2012, 10:00 | Sanba |
| | | 356 | Sep. 12, 2003, 20:00 | Maemi |
| Samcheonpo | 2 | 352 | Aug. 30, 2015, 22:00 | n/a |
| | | 350 | Oct. 28, 2015, 09:00 | n/a |
| | | 350 | Nov. 27, 2015, 10:00 | n/a |
| Geoje | 11 | 270 | Sep. 17, 2012, 09:00 | Sanba |
| | | 259 | Sep. 17, 2012, 10:00 | Sanba |
| | | 255 | Jan. 4, 2006, 09:00 | n/a |
| Gwangyang | 6 | 479 | Sep. 17, 2012, 10:00 | Sanba |
| | | 443 | Sep. 17, 2012, 11:00 | Sanba |
| | | 441 | Aug. 1, 2014, 22:00 | n/a |
| Yeosu | 52 | 440 | Aug. 18, 1966, 23:00 | n/a |
| | | 430 | Sep. 14, 1966, 21:00 | n/a |
| | | 129 | Aug. 17, 1966, 22:00 | n/a |

155 As can been seen from Table 7, above, the three highest recorded sea levels at each south coast tidal-gauge station corresponded with the occurrence of typhoons in 20 out of 30 cases. The dates and times of the three highest sea levels observed during Busan's entire observation period (1962-2019) all coincided with Typhoon Maemi passing out of the area. As well as US$35 billion in property damage, Typhoon Maemi caused 135 casualties in Busan and nearby cities (National Typhoon Center 2011). However, other typhoons – notably including Thelma, Samba, and Megi – also caused very

160 significant damage, as shown in Table 1.

### 1.3 Research objective

The objective of this study is to the estimate the probability of the risk, in years, of typhoon-induced high water levels in Busan. To that end, it adapts Lopeman et al.'s (2015) clustered separated peaks-over-threshold method (CSPS), which

165 provides statistical analysis of extreme values in long time series of natural phenomena. As such, CSPS can provide useful guidance to those tasked with preparing for natural disasters on the Korean Peninsula, and perhaps especially on its southern coast. The findings from this research are therefore expected provide a viable method of predicting economic losses associated with typhoons, and corresponding models for managing emergency situations arising from natural disasters, that

can be used by South Korea's government agencies, insurance companies, and construction industry. And, although this
170  study focuses on a specific city-region, the proposed probabilistic methodologies should be applicable to other coastal
regions in South Korea and around the world.

## 2 Literature review

### 2.1 Prior studies of Typhoon Maemi

175  Most previous studies devoted to avoiding or reducing natural-disaster damage in South Korea have focused on storm
characteristics, such as storm track, rainfall, radius, and wind-field data. Their typical approach has been to create synthetic
storms that can be utilized to predict real storms' paths and estimate the extent of the damage they would cause.

Kang (2005) investigated the inundation and overflow caused by Maemi at one location near the coast, using a site survey
and interviews with residents, and found that the storm surge increased water levels by 80%. Using a numerical model, Hur
180  et al. (2006) estimated storm surges at several points in the Busan area caused by the most serious typhoons, including Sarah,
Thelma, and Maemi. Having established that Typhoon Maemi was accompanied by the highest storm surge, they then
simulated storm surges as a means of investigating the tidal characteristics of Busan's coast, and created virtual typhoons to
compare against the actual tracks of Sarah, Thelma, and Maemi. When these virtual typhoons followed the track of Typhoon
Maemi, the simulated storm surge was higher than those produced when they followed the tracks of Sarah and Thelma.

185  Lee et al. (2008), using atmospheric-pressure and wind profiles of Typhoon Maemi, introduced a multi-nesting grid model to
simulate storm surges. To check its performance, they used numerical methods for tidal calibration and to assess the
influence of open-boundary conditions and typhoon paths. This yielded two key findings. First, the location of a typhoon's
center was the most critical factor when calculating storm surges; and second, the track of the typhoon was a secondary, but
still important, factor in storm-surge prediction. However, Lee et al.'s research was limited by the fact that only recorded
190  storm tracks were used, meaning that their simulations could not calculate storm surges from any other possible tracks.
Similarly, Chun et al. (2008) used a numerical model, combined with moving boundary conditions to explain wave run-up,
to simulate the storm surge of Typhoon Maemi, but using data from the coastal area of Masan: a city near Busan that was
also damaged by the storm. The inundation area and depth predicted by that model were reasonably well correlated with the
actual area and depth arrived at via a site survey. And Kim and Suh (2018) created 25,000 random storms by modifying an
195  automatic generation tool, the Tropical Cyclone Risk Model, and simulated surge elevations for each of them. The tracks of
these simulated storms had similar patterns to those of actual typhoons in South Korea.

However, while past research on Typhoon Maemi has used such input data as atmospheric pressure, wind fields, typhoon
radius, storm speed, latitude, longitude, and tidal-gauge data, the tidal gauge data has not been used for estimating
exceedance probability of storm surge. For instance, Kim and Suh (2018) did not perform surge modeling or frequency
200  analysis in the time domain; and, although Chun et al.'s (2008) numerical models provided valuable predictions of

inundation area and depth, they did not take account of tidal fluctuation which, if combined with increased water levels, would have yielded different results.

## 2.2 Return period estimates for Hurricane Sandy

While no prior research has estimated return periods for typhoons, some has done so for hurricanes. For example, Lopeman
205 (2015) used tidal-gauge data to estimate the return period for Hurricane Sandy, which struck the United States in 2012. Talke et al. (2014) also used tidal-gauge data, to study the storm-surge hazard in New York Harbor over a 37-year period, and found that its pattern underwent long-term changes due to sea-level rises caused in part by climate change. However, Talke et al. did not estimate a specific return period for Hurricane Sandy.

Lin et al. (2010), on the other hand, did estimate the return periods of storm surges related to tropical cyclones in the New
210 York City area, with that for Sandy in Lower Manhattan being 500 years within a 95% confidence interval (CI), i.e., approximately 400-700 years. Lin et al. (2012) later conducted a similar analysis using computational fluid dynamics Monte Carlo simulations that took account of the randomness of the tidal-phase angle. This approach yielded a return period of 1,000 years with a 90% CI (750-1,050 years). The former study can be considered the less accurate of the two, because it did not consider different surge-height possibilities at different time windows within the tidal cycle.

215 Hall and Sobel (2013) developed an alternative method to estimate Sandy return periods, based on the insight that this storm's track could have been the primary reason for the damage it caused in Lower Manhattan and other parts of the city. Specifically, they argued that Sandy's perpendicular impact angle with respect to the shore as it passed to the south of Manhattan's port was of critical importance, based on an analysis of the tracks of other hurricanes of similar intensity. They estimated the return period for Sandy's water level to be 714 years within a 95% CI (435-1,429 years).

220 Zervas (2013) estimated the return periods for extreme events using monthly mean water-level data from the U.S. National Oceanographic and Atmospheric Administration, recorded at the tidal-gauge station in Battery Park, New York. Using generalized extreme-value (GEV) distribution and maximum-likelihood estimation (MLE) methods, Zervas calculated that the return period for Sandy's peak water level was 3,500 years; but sensitivity analysis suggested that the estimated results were probably inaccurate, given the GEV fit's sensitivity to the range of years used. Once Sandy was excluded, the return
225 period was 60,000 years. This difference in results suggests that GEV distribution of the yearly maximum water level is not a realistic method for estimating extreme events in the New York Harbor area.

Building on their own past research, Lopeman (2015) were the first researchers to estimate Sandy's return period using tidal-gauge data. They proposed that CSPS should be used, and that tide fluctuation, surge, and sea-level rise should all be dealt with separately, as of these three phenomena, only surge is truly random. This approach led them to calculate the return
230 period as 103 years with a 95% CI (38-452 years).

The sharp differences in the results of the past studies cited above are due to wide variations in both the data they used and their assumptions. The present study therefore applies all of the methods used in previous studies of Hurricane Sandy's return period to estimate that of Typhoon Maemi, and in the process, establishes a new model.

### 2.3 Extreme value statistics

235  **2.3.1 Generalized extreme value distribution**

Extreme events are hard to predict because data points are so few, and predicting their probability is particularly difficult due to their asymptotic nature. Extreme-value probability theory deals with how to find outlier information, such as maximum or minimum data values during extreme situations. Examining the tail events in a probability distribution is very challenging. However, it is considered very important by civil engineers and insurers, due to their need to cope with low-probability,

240  high-consequence events. For example, the designs and insurance policies of bridges, breakwaters, dams, and industrial plants located near shorelines or other flood-prone areas should account for the probability, however low, of major flooding. Various probability models for the study of extreme events could potentially be used in the present research, given that its main theme is the extreme high water levels caused by typhoons. Extreme-value theories can be divided into two groups, according to how they are defined. In the first, the entire interval of interest is divided into a number of subintervals. The

245  maximum value from each subinterval is identified as the extreme value for it, and then the entirety of these extreme values converges into a GEV distribution. In the second group, values that exceed a certain threshold are identified as extreme, and converge to a generalized Pareto distribution (GPD). In the following two subsections, we will discuss the block maxima (BM) and the peaks-over-threshold (POT) methods, as illustrations of these two groups, respectively (Coles 2001).

*Block maxima method*

250  The BM approach relies on the distribution of the maximum extreme values in the following equation,

$$M_n = \max\{X_1, \dots, X_n\} \tag{1}$$

where the $X_n$ series, comprising independent and identically random variables, occurs in order of maximum extreme values; n is the number of observations in a year; and $M_n$ is the annual maximum.

Data is divided into blocks of specific time periods, with the highest values within each block collectively serving as a

255  sample of extreme values. One limitation of this method is the possibility of losing important extreme-value data because only the single largest value in each block is accounted for, and thus, the second-largest datum in one block could be larger than the highest datum in another.

*Peaks-over-threshold method*

The POT method can address the above-mentioned limitations of BM, insofar as it can gather all the data points that exceed

260  a certain prescribed threshold, and use limited data more efficiently because it relies on relatively larger or higher values instead of the largest or highest ones. All values above the threshold – known as exceedances – can be explained by the differentiated tail-data distribution. The basic function of this threshold is to assort the larger or higher values from all data; and the set of exceedances constitutes the sample of extreme values. This means that, although POT can capture potentially important extreme values even when they occur close to each other, selecting a threshold that will yield the best description

265  of the extreme data can be challenging (Bommier 2014): if it is set too high, key extreme values might be lost, but if it is set

too low, values that are not really extreme may be included unnecessarily. Determining appropriate threshold values thus tends to require significant trial and error, and various studies have proposed methods for optimizing such values (Lopeman et al. 2015; Pickands 1975; Scarrott and Macdonald 2012). Pickands, for instance, suggested that independent time series that exceed enough high thresholds would follow GPD asymptotically, thus avoiding the inherent drawbacks of BM.

270   Equation (2) explains the distribution function F of exceedance,

$$F_\theta(x) = P\{X - \theta \leq x | X > \theta\}, \quad x \geq 0 \tag{2}$$

where θ is the threshold and X is a random variable.

Also, as shown in Equation (3), $F_u$ can be defined by conditional probabilities:

$$F_\theta(x) = \begin{cases} \frac{F(\theta+x)-F(\theta)}{1-F(\theta)} & \text{if } x \geq 0 \\ 0 & \text{else} \end{cases} \tag{3}$$

275   According to Bommier (2014), the distribution of exceedances $(Y_1, \ldots, Y_{n_\theta})$ can be generalized by GPD with following assumption: When $Y = X - \theta$ for $X > \theta$, and $X_1, \ldots, X_n$, $Y_j = X_i - \theta$ can be described with i which is jth exceedance, $i = 1, \ldots, n_\theta$.

Equation (4) expresses the GPD,

$$G_x(x; \xi, \sigma, \theta) = \begin{cases} 1 - \left(1 + \xi \frac{(x-\theta)}{\sigma}\right)^{1/\xi} & \xi \neq 0 \\ 1 - \exp\left(-\frac{(x-\theta)}{\sigma}\right) & \xi = 0 \end{cases} \tag{4}$$

280   with x being independent and identically random variables; σ, the scale; ξ, the shape; and θ, the threshold. All values above θ are considered tail data (extreme values). When calculating the return level that is exceeded once every N years (N-year return periods $x_N$), Equation (5) describes the probability of exceedance over a threshold.

$$P\{X > x | X > \theta\} = \left[1 + \xi \left(\frac{x-\theta}{\sigma}\right)\right]^{-1/\xi} \tag{5}$$

If the exceedances above the threshold are rare events λ (as measured by number of observations per year), we can

285   expect $P(X > \theta)$ to follow Poisson distribution. The mean of exceedance per unit of time (ŷ) describes that distribution.

$$P(X > \theta) = \frac{\gamma}{\lambda} \tag{6}$$

In other words, γ can be estimated by dividing the number of exceedances by the number of years in the observation period. Combining the POT and Poisson processes with GPD allows us to describe the conditional probability of the extreme values that exceed the designated threshold, as per Equation (7) (Lopeman et al. 2015):

290   $$P(A|B) = \frac{P(A \cap B)}{P(B)} \tag{7}$$

And when Bayes' theorem is applied to the role of GPD in conditional probability, we can rewrite Equation (7) as follows:

$$G_X(x) = \frac{P(\theta < X < x)}{P(X > \theta)} \tag{8}$$

## 3 Research methods

### 3.1 Data processing

#### 3.1.1 Storm surge data collection method

To determine the height of surges from publicly available KHOA data, it is first necessary to predict sea levels. Equation (9) explains the relationship among observed water level, predicted water level, tidal fluctuation height, and residual (surge) at time $t_i$,

$$Y_i = X_i + S_i \tag{9}$$

where i = 1, 2, …, n; n is the time series of the input dataset; $X_i$, the predicted water height at $t_i$; $Y_i$, the observed water height at $t_i$; and $S_i$, the surge height.

#### 3.1.2 Separation of tidal gauge data (harmonic analysis)

In this study, a standard harmonic analysis was performed to calculate predicted sea level height based on hourly data. First, this technique was used to estimate the tidal components from the total seawater-level data, allowing residuals to be isolated so that surge data could be calculated once sea-level rise had been estimated. Second, the estimated constituents were used to predict tidal fluctuations in the years simulated via Monte Carlo. Then, the TideHarmonics package in R (Stephenson 2017) was used for the estimation of tidal components, as detailed below.

Consider the time series Y(t) of total water levels, with t denoting time in hours. The representation of the tidal component with M harmonic constituents is computed as

$$\hat{Y}(t) = Z + \sum_{m=1}^{M} A_m \cos\left(\frac{\pi}{180}(\omega_m t - \psi_m)\right) \tag{10}$$

where $\omega_m$ is the angular frequency of the m-th component in degrees per hour. The $2M + 1$ parameters to be estimated are the amplitudes $A_m$; the phase lags $\psi_m$ in degrees; and the MSL, Z.

To account for long astronomical cycles (LAC), nodal-correction functions for both the amplitude and phase are used. With these corrections, the tidal component takes the form

$$\hat{Y}_{LAC}(t) = Z + \sum_{m=1}^{M} H_m f_m(t) \cos\left(\frac{\pi}{180}(\omega_m t - g_m + u_m(t) + V_m)\right) \tag{11}$$

where $f_m(t)$ and $u_m(t)$ represent the nodal corrections for the amplitude and phase, respectively. In this new formulation, the amplitude and phase parameters to be estimated are denoted by $H_m$ and $g_m$ (in degrees). Finally, $V_m$ is the reference signal, by which the phase-lag $g_m$ is calculated and set to refer to the origin $t = 0$.

The summation term in $\hat{Y}_{LAC}(t)$ can alternatively be written as

$$\sum_{m=1}^{M} \beta_{m,1} f_m(t) \cdot \cos\left(\frac{\pi}{180}(\omega_m t + u_m(t) + V_m)\right) + \sum_{m=1}^{M} \beta_{m,2} f_m(t) \cdot \sin\left(\frac{\pi}{180}(\omega_m t + u_m(t) + V_m)\right) \tag{12}$$

where $\beta_{m,1} = H_m \cos(g_m)$ and $\beta_{m,2} = H_m \sin(g_m)$. What is gained from this new representation is a linear function with respect to the parameters $\beta_{m,1}$ and $\beta_{m,2}$ that need to be estimated; and hence, a linear regression can be used. Given the large

timespan covered by the data, M = 60 harmonic tidal constituents were estimated, and a constant mean sea level Z was assumed across all years of data available.

### 3.1.3 Observed, predicted and residual water levels

Because observed sea level usually differs from predicted sea level, Figure 5 displays the former at Busan's tidal-gauge station in blue, as calculated through harmonic analysis. Predicted sea levels at the same location are shown in green, and surge height in red.
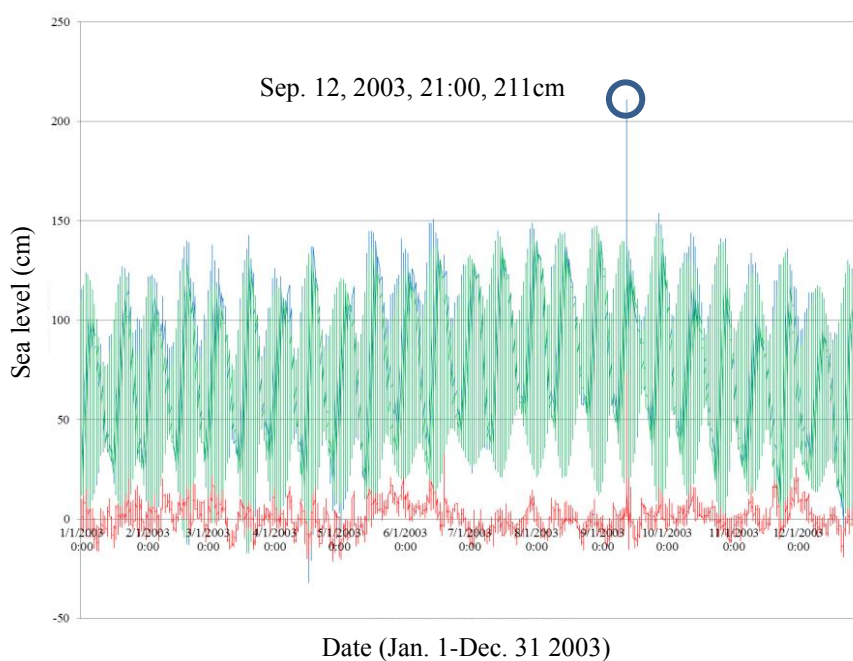
Figure 5. Observed (blue), predicted (green), and residual (red) water levels in Busan, South Korea, 2003

As the figure indicates, the highest overall water level coincided with the highest surge during Typhoon Maemi. Figure 6 presents the observed (blue), predicted (green), and surge (red) levels at the time of the highest sea level recorded at Busan, i.e., at 21:00 on September 12, 2003. Given a total water height of 211cm, the surge height was calculated as 73.35cm.
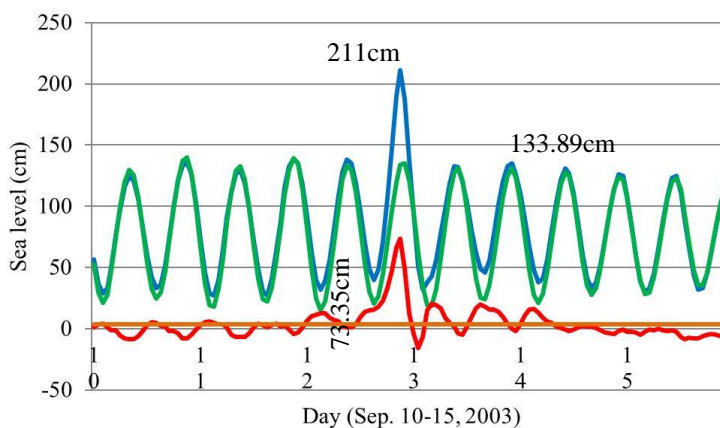
Figure 6. Observed (green), predicted (blue), and residual (red) water levels at Busan during Typhoon Maemi

### 3.2 Data analysis

#### 3.2.1 Threshold and target rate selection

At a given target annual rate – i.e., number of storms per year – the algorithm proposed by Lopeman et al. (2015) (Figure 7) computes the threshold such that this rate approximates the resulting yearly number of exceedance clusters. In this case, an exceedance cluster is a set of consecutive surge observations that lie above the threshold. Hence, rather than choosing an "ideal" threshold according to some criterion or other, the algorithm simply finds the threshold that forces a chosen target rate to occur. Accordingly, a study of this kind could set its target rate as the average rate observed over a given period, or as a value that the authors find reasonable in light of their knowledge of historical data for their focal area.

Next, the algorithm iteratively updates the threshold to allow a computationally intensive, but not exhaustive, exploration of possible threshold values between its minimum value (i.e., here, minimum observed surge height) and its maximum one (i.e., maximum observed surge height). Specifically, it first sets the threshold to 0cm, and then iteratively overwrites it according to the following steps.

(1) The exceedance clusters produced at a given iteration and given threshold are identified, and the resulting annual storm rate computed.

(2) If the annual storm rate arrived at in step (1) is equal to, or about equal to, the chosen target, then the threshold from the previous iteration is the result, and the algorithm is stopped.

(3) If the annual storm rate arrived at in step (1) is not close enough to the chosen target…

  (a) …but is smaller than the target rate, then the threshold from the previous iteration is the result, and the algorithm is stopped; or

(b) …but is larger than the target rate, then a vector collecting the maximum height of the clusters is built and sorted in descending order. The threshold is then updated by setting it as equal to the C-th element of this vector, where C is the integer closest to the value of 54 (the number of years covered by the dataset) multiplied by the target rate. This updated threshold is used in the next iteration of the algorithm, and steps (1) through (3) are repeated.

360
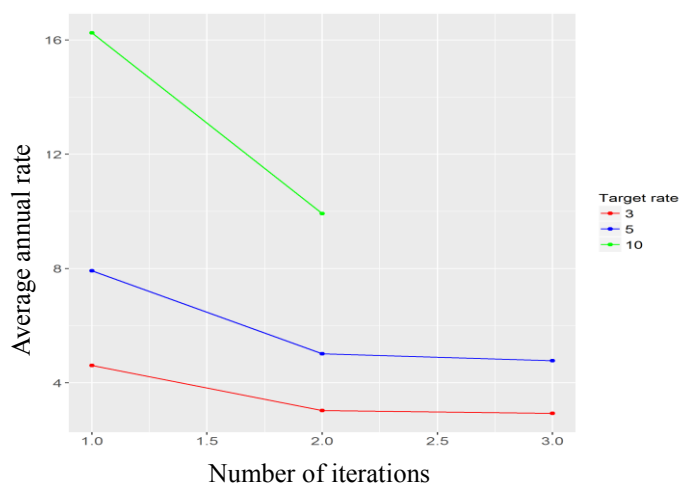
Figure 8. Iterative process of threshold selection (1 of 3)

365
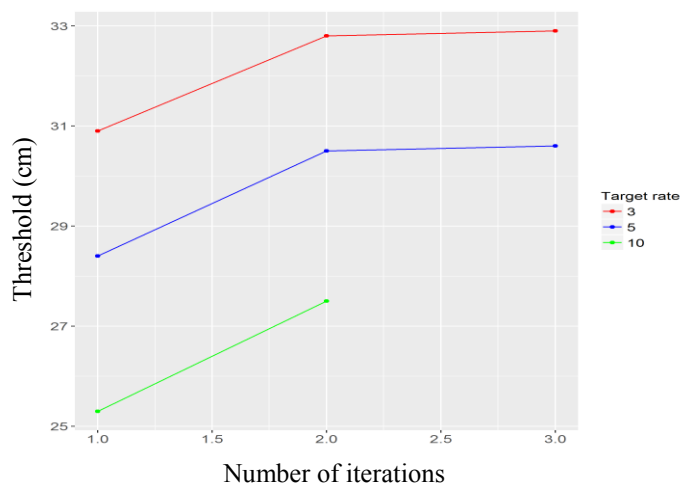
Figure 9. Iterative process of threshold selection (2 of 3)
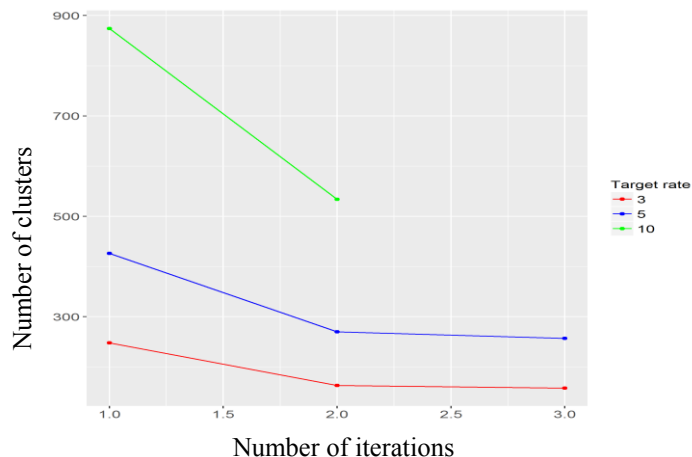
Figure 10. Iterative process of threshold selection (3 of 3)

As shown in Figures 8, 9, and 10, the threshold algorithm (Figure 7) achieved convergence relatively quickly for all three
370    target rates selected, with the number of iterations required for convergence ranging from three (with a target rate of 3) to
five (with a target rate of 10).
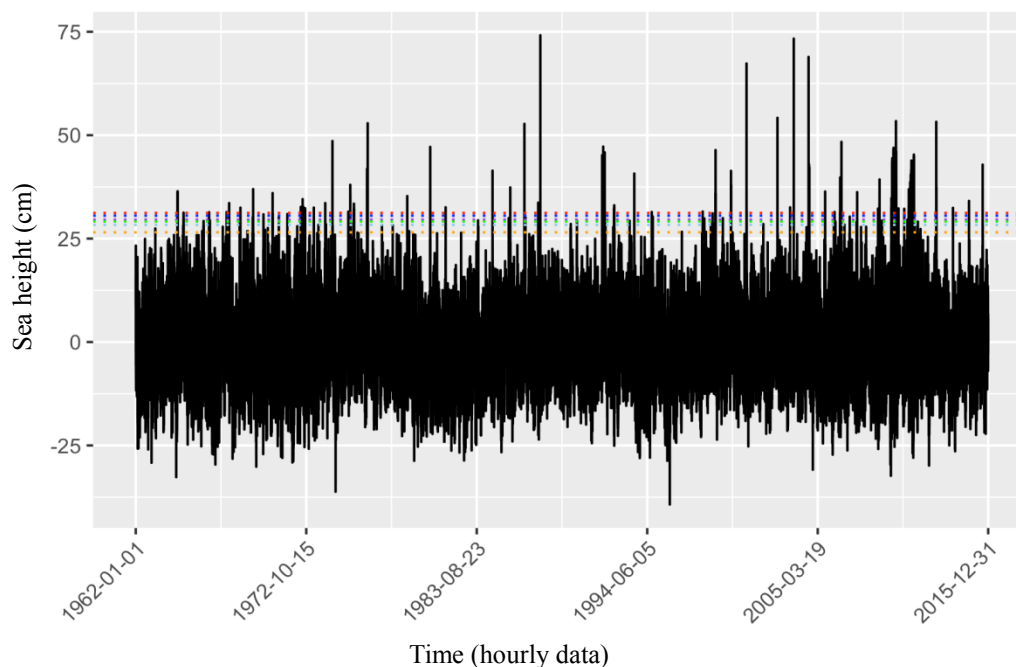
Figure 11. Various thresholds considered

375  Figure 11 displays six possible thresholds. The first, of 31.2cm, was based on a target rate of 3.5, and 189 clusters, and is shown in red. The dark-blue line represents the second threshold, of 30.54cm, (target rate=4, clusters=217); the purple, a threshold of 29.56cm (target rate=4.5, clusters=246); the green, a threshold of 29.15cm (target rate=5, clusters=274); the sky-blue, a threshold of 28.33cm (target rate=6, clusters=324); and the orange, a threshold of 26.53cm (target rate=8, clusters=431).

380  **3.2.2 Clustering of the storm surge data (Relationship among target rate, threshold and clusters)**

Figure 11 shows that, as expected, when the target rate increases, the threshold decreases, and as the threshold decreases, the number of clusters (i.e., storm events) increases. Conversely, the lower the target rate, the lower the number of clusters and the higher the threshold. Thus, if the desired number of storms is three per year, the algorithm will converge in three iterations and set the threshold level to 32.01cm; this results in a total of 164 storm events (clusters) over the timespan

385  covered by our data. Conversely, if the desired target rate is 10 storms per year, the threshold is significantly lower (25.43cm), and the total number of storm events more than trebles, to 539 clusters. Figures 12, 13, and 14 show the stages of the clustering of surges when the target rate is set to five, the threshold is 29.15cm, and the number of clusters is 274. (it should be noted that Figure 12 indicates only the number of surges, because of the difficulty of visually representing all surge dates and times.)
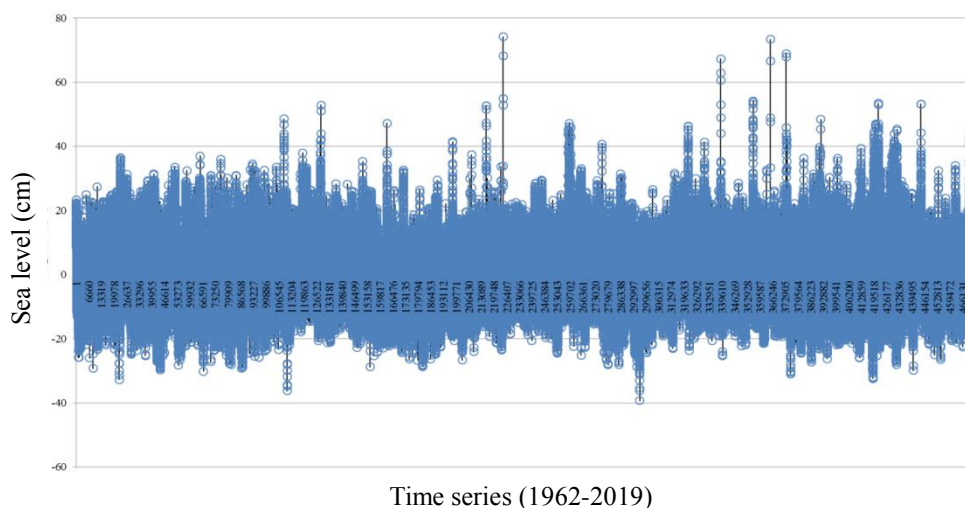
390

Figure 12. Data from Busan tidal-gauge station, before application of any thresholds
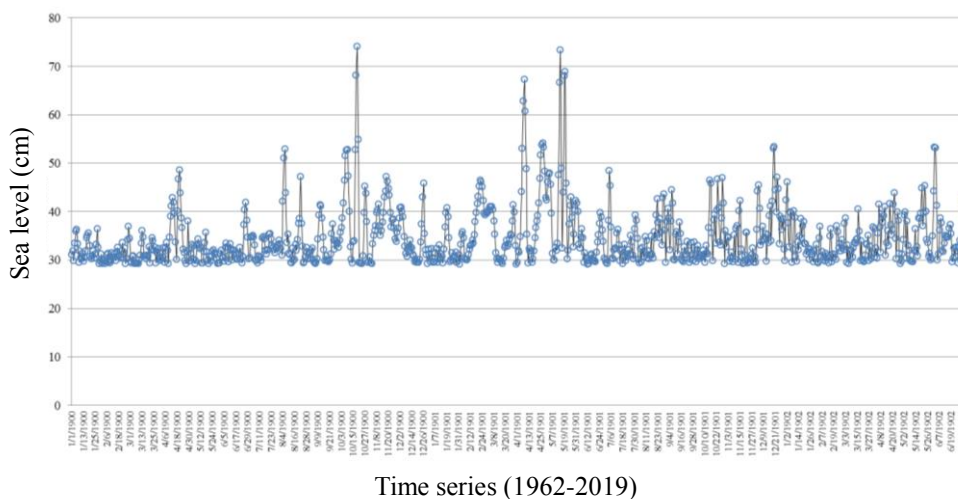
Figure 13. Surges at Busan above a threshold of 29.15cm, before clustering

395
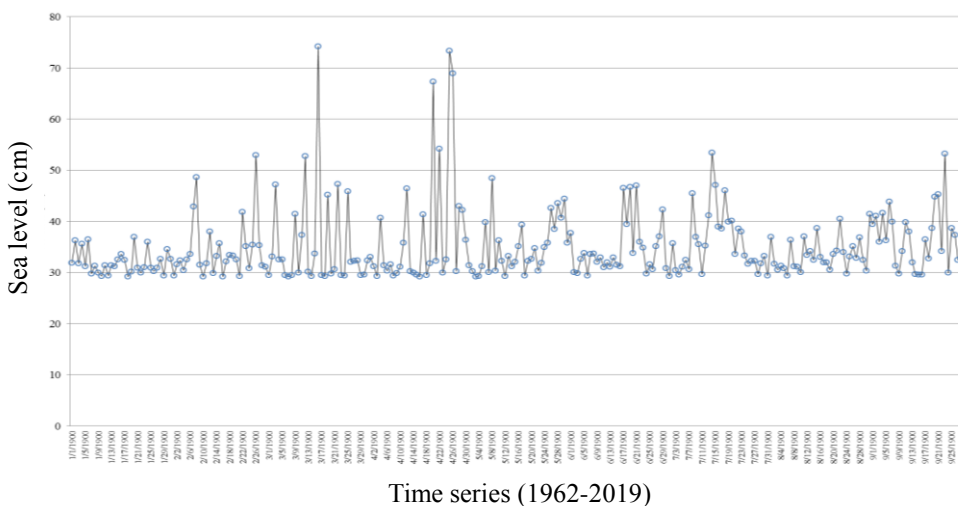
Figure 14. Surges at Busan above a threshold of 29.15 cm, after clustering

### 3.2.2 Relationship among storm surge parameters

*Storm-surge parameters*

Storm surges are characterized by four major parameters: peak time, peak height, duration, and rise ratio. Peak time follows

400    a gamma distribution because POT produces a Poisson process of exceedance occurrence, and the waiting times between

consecutive exceedances in a Poisson process are, by definition, exponentially distributed (Lopeman et al. 2015). For the

peak times (interarrival times), this study therefore uses a gamma (exponential) distribution, under the common POT assumption that the arrival maxima of exceedance clusters are regulated by a Poisson process.

For peak height, on the other hand, GPD is typically used, because some representation-theorem results from extreme-value statistics indicate that, if the cluster maxima follow a Poisson process, then the intensity – in this case, height – of the cluster peaks follows a GPD distribution (Lopeman et al. 2015; Zhong et al. 2014). However, a Weibull distribution has been applied to peak storm-surge heights in this study because it fits the data better, especially with regard to the right-hand tail.

Because the rise ratio does not appear to be evenly distributed along the interval [0, 1], a beta distribution was used because the rise ratio is by definition between 0 and 1, and the beta distribution is commonly used to model continuous random variables that occur within that range (Lopeman et al. 2015).

Duration follows a lognormal distribution, which was used for the following two reasons, previously articulated by Lopeman et al. (2015). First, it models a continuous and positive random variable: duration, by definition, is positive. And second, it is quite flexible: i.e., having two parameters, it can fit the data better than other distributions with just one, such as exponential distribution.

*Parameter interrelationships*

Figures 14, 15, and 16 indicate that there is no clear relationship between rise ratio, on the one hand, and either duration or exceedance, on the other. However, peak exceedance and cluster duration appear to have a linear relationship.
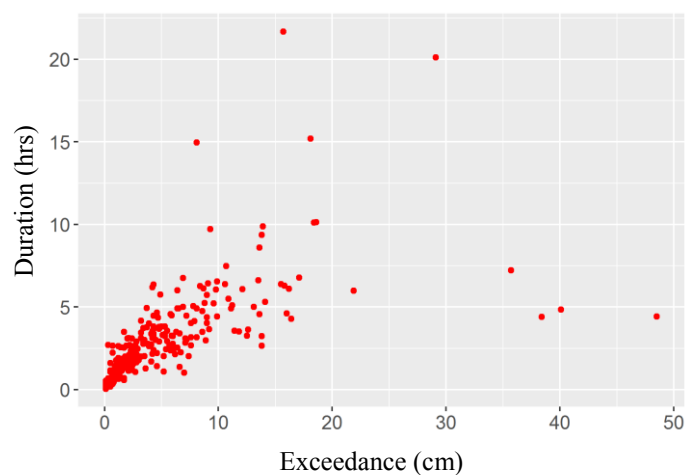
Figure 14. Relationship between exceedance and duration
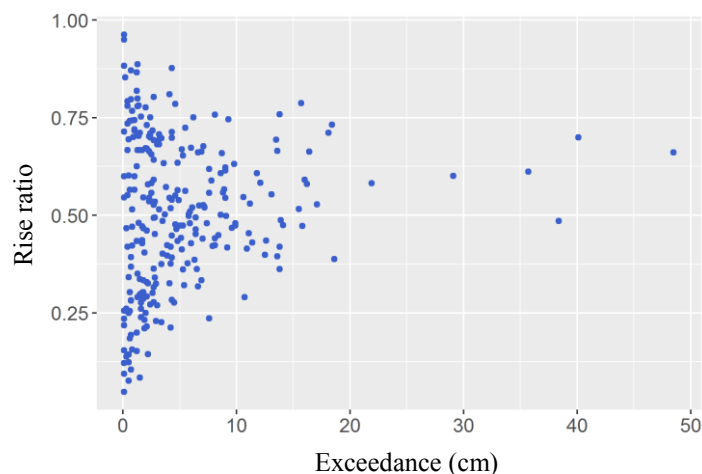
Figure 15. Relationship between exceedance and rise ratio
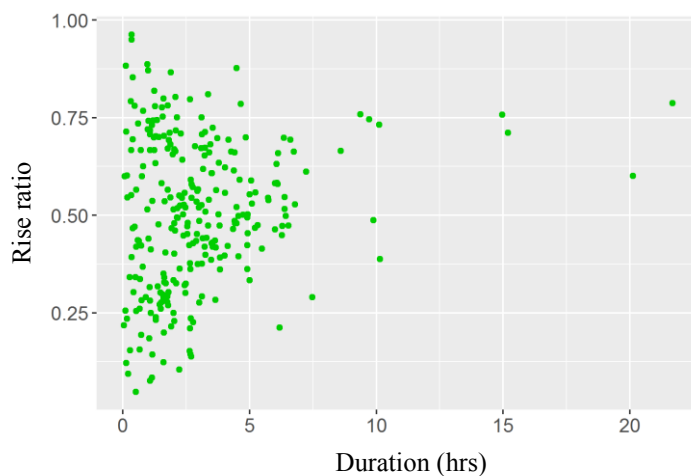
Figure 16. Relationship between duration and rise ratio

## 4 Results and analysis

### 4.1 Storm surge simulation

#### 4.1.1 Fitting this study's statistical model to the actual surge data

After finding the threshold that results from a given target rate, we computed interarrival times, rise ratios, peak height, and cluster duration for each exceedance cluster. These figures were then grouped by season (the year being divided for this purpose into a cold season lasting from December through May and a warm season), and such groups were used to estimate

the parameters of the statistical model via MLE. For the reasons given in the previous section, the interarrival times for each season were fitted with an exponential distribution; the rise ratios with a beta distribution; and the peak heights with a Weibull distribution in which the location parameter was equal to the threshold. Detailed descriptions of how we applied each of these methods are provided in turn below.

435 *Maximum likelihood estimation*

If we assume that an independent and identically distributed data sample $(x_1, \ldots, x_n)$ is observed from a population with a distribution of interest parametrized by an unknown variable $\theta$, which the study wants to estimate, the MLE estimator $\hat{\theta}_{MLE}$ is defined as:

$$\hat{\theta}_{MLE}(x_1, \ldots, x_n) = argmax_{\theta_0} \prod_{i=1}^{n} f(x_i; \theta_0), \tag{13}$$

440 where $f(\cdot; \theta)$ denotes the probability-density function of the distribution of interest, parametrized by $\theta_0$. The distributions of interest for the data in this study were chosen as follows:

(1) $T_i \sim Exponential(\lambda)$, where $T_i$ denotes the interarrival time between the peak of the $i-1$th cluster and the peak of the $i$-th cluster. This distributional assumption is equivalent to assuming that a Poisson process governs peak-surge arrivals.

445 (2) $\Phi_i \sim Beta(\alpha, \beta)$, where $\Phi_i$ denotes the rise ratio of the $i$-th cluster.

(3) $\prod_i \sim GPD(\xi, \sigma, \theta^*)$, where $GPD$ denotes the generalized Pareto distribution, $\prod_i$ the peak surge height of the $i$-th cluster, and $\theta^*$ the selected threshold.

For the exponential distribution (i.e., interarrival times), the exact solutions of the maximization problem stated above can be derived in closed form. For the GPD distribution (i.e., peak exceedances) and the beta distribution (i.e., rise ratios), the

450 problem is solved numerically. A full description of the estimation algorithm MLE for interarrival times, rise ratios, and peak exceedances is detailed below.

(1) Input:

(a) Observed interarrival times $t_1, \ldots, t_C$ of the clusters' surge peaks.

(b) Observed rise ratios $\phi_1, \ldots, \phi_C$.

455 (c) Observed peak surge heights $\gamma_1, \ldots, \gamma_C$.

(d) Number of clusters $C$.

(e) Threshold rate $\theta^*$.

(2) Output:

Maximum-likelihood estimates of the model parameters $\hat{\lambda}_{MLE}, \hat{\alpha}_{MLE}, \hat{\beta}_{MLE}, \hat{\xi}_{MLE},$ and $\hat{\sigma}_{MLE}$.

460 (3) Procedure:

(a) Compute the MLE estimate $\hat{\lambda}_{MLE}$ for the exponential interarrival rate $\lambda$ as:

$$\hat{\lambda}_{MLE} = (\sum_{c=1}^{C} t_c)^{-1} \tag{14}$$

(b) Compute the MLE estimates $\hat{\alpha}_{MLE}$ and $\hat{\beta}_{MLE}$ for the beta parameters $\alpha$ and $\beta$, by numerically solving the following first-order equations,

465

$$C\left(\psi(\hat{\alpha}_{MLE} + \hat{\beta}_{MLE}) - \psi(\hat{\alpha}_{MLE})\right) + \sum_{c=1}^{C} \log \phi_i = 0; \qquad (15)$$

$$C\left(\psi(\hat{\alpha}_{MLE} + \hat{\beta}_{MLE}) - \psi(\hat{\alpha}_{MLE})\right) + \sum_{c=1}^{C} \log(1 - \phi_i) = 0, \qquad (16)$$

in which $\psi(\cdot)$ denotes the digamma function.

(c) Compute the MLE estimates $\hat{\xi}_{MLE}$ and $\hat{\sigma}_{MLE}$ for the GPD parameters $\xi$ and $\sigma$. Further details on this estimation can be found in the documentation provided by the ismev package (Heffernan and Stephenson 2012).

470

(d) Return the MLE estimates $\hat{\lambda}_{MLE}, \hat{\alpha}_{MLE}, \hat{\beta}_{MLE}, \hat{\xi}_{MLE}, \hat{\sigma}_{MLE}$ to step 3(a), above.
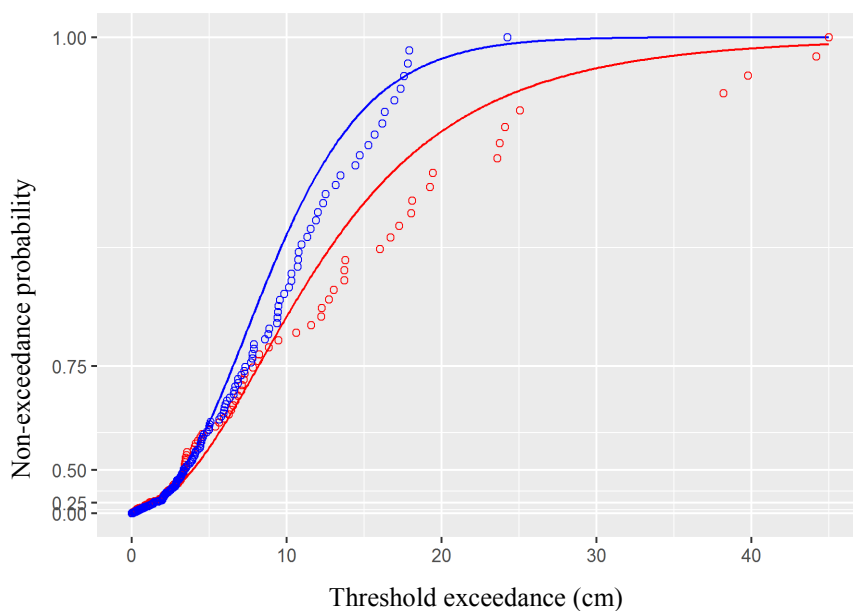
Figure 17. Generalized Pareto distribution at target rate=5

475

480
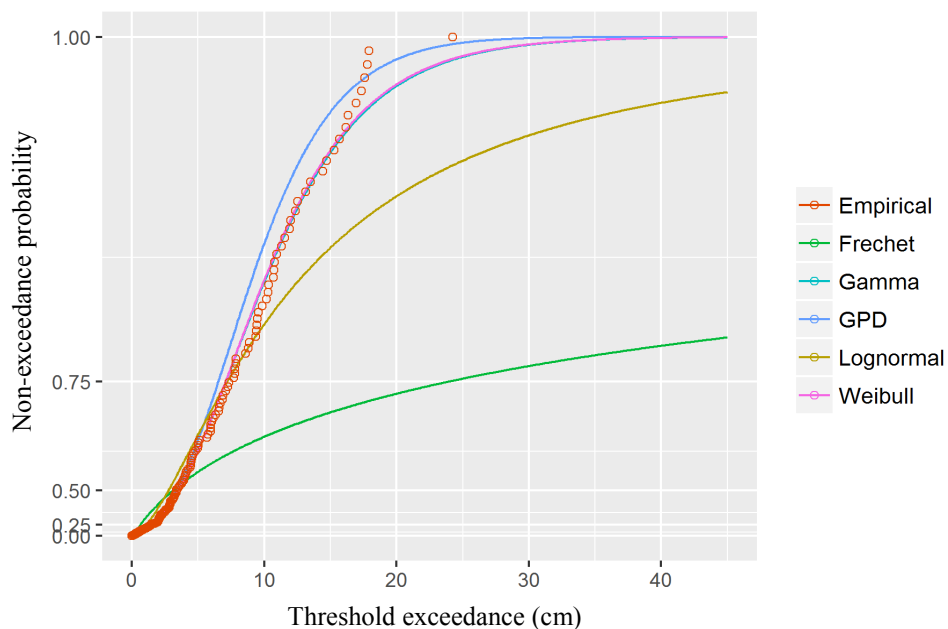
485                   Figure 18. Fits of six types of distributions, cold season, target rate=5
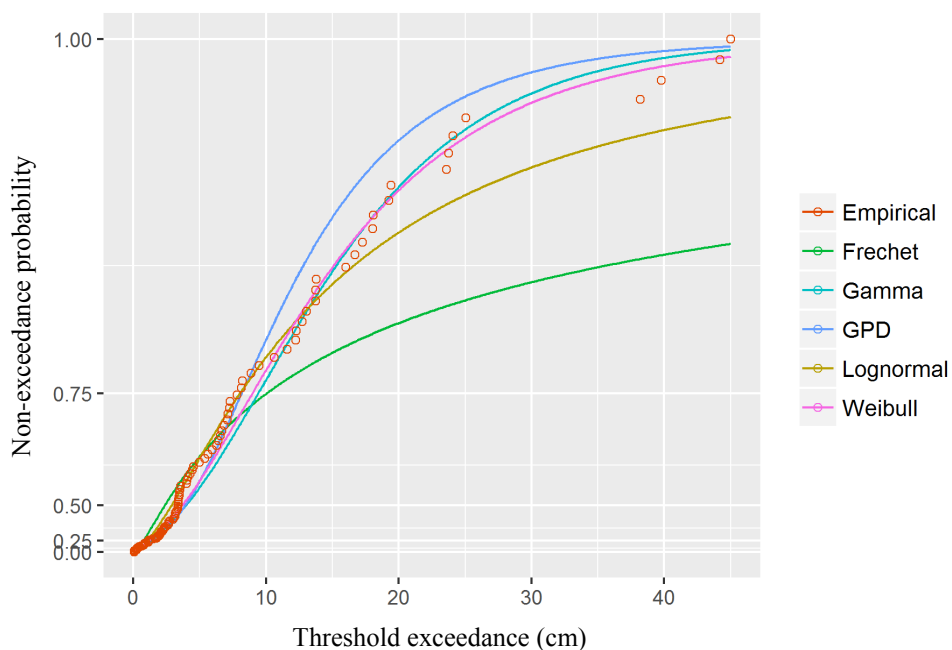
Figure 19. Fits of six types of distributions, warm season, target rate=5

Figure 17 shows the GPD cumulative-distribution function as estimated by maximum likelihood, and the empirical
490 distribution function, with the latter shown as dots. Each dot represents the observed proportion of exceedances below a
certain height in a given season (blue: cold season, red: warm season), while the corresponding value on the fitted line of the
same season gives the probability that the exceedances are below that height, per the estimated GPD distribution.

Figures 18 and 19 indicate that the Gamma and Weibull distributions fitted to the data for the cold and warm seasons via
maximum likelihood are better than the GPD distribution across a variety of target rates, as measured by mean square error
495 (MSE). This confirms the conclusions suggested graphically by the plots.

**5 Conclusion**

Typhoons cause numerous fatalities and immense property damage, and their frequency has recently been increasing.
Nevertheless, comprehensive typhoon risk assessments are not yet sufficiently developed to estimate either the damage
levels from such events, or the probability of their occurrence. If they are to effectively plan for typhoons, governments and
500 the insurance industry will need accurate estimates of both. Prompted by the high levels of damage inflicted by the high
surge during South Korea's most severe typhoon, Maemi, this research has estimated the risk of storm surges through non-
exceedance probability using a maximum-likelihood method. Its findings afford us an opportunity to compare various
statistical probability models of typhoon-induced surges, which in turn can enhance the quality of estimation of the risk of
these natural hazards. Non-exceedance probability can also be a useful, geographically sensitive tool for government
505 agencies, insurance companies, and construction companies conducting risk assessments, setting insurance prices, preparing
safety guidelines, and setting policies aimed at reducing typhoon-related damage and financial losses.

Even though the present research investigated various non-exceedance probability distributions of typhoon-driven storm
surges, it only used a single extreme event in a specified region. As such, its findings may not be applicable to other regions,
each of which has its own unique weather conditions, geographic features, and tidal characteristics. Future research should
510 therefore include tidal and environmental data from a range of different regions and various extreme events to confirm the
present study's findings. Also, various natural-hazards indicators and environmental factors such as wind speed, pressure,
rainfall, landslides, distance to waterways, and so forth may be useful variables in estimating the exceedance probabilities of
typhoons and other natural hazards, and thus be beneficial to risk assessment and mitigation.

Return periods based on various non-exceedance probability models should also be considered in future research, since
515 elaborated return-period estimation can be utilized for better disaster relief and emergency planning. Advanced statistical
methods such as Monte Carlo simulation, as well as deep-learning techniques, can be applied to make typhoon return-period
estimates even more accurate.

**Acknowledgement**

This research was funded by Hanyang University ERICA.

520 **References**

1)  Esther Bommier. Peaks-Over-Threshold Modelling of Environmental Data. *Department of Mathsmatics, Uppsala University*, 2014.

2)  Jae-Young Chun, Kwang-Ho Lee, Ji-Min Kim, and Do-sam Kim. Inundation Analysis on Coastal Zone around Masan Bay by Typhoon Maemi. *Journal of Ocean Engineering and Technology*, 22(3), 8-17, 2008.

525 3)  Stuart Coles. An *introduction* to statistical modeling of extreme values. *Springer*, 2001

4)  Timothy M. Hall and Adam H. Sobel. On the impact angle of Hurricane Sandy's New Jersey landfall. *Geophysical Research Letters*, 40(10), 2312–2315, 2013.

5)  Yunji Hwang. Stochastic analysis of storm-surge induced infrastructure losses in New York City. *Ph. D dissertation*, *Columbia University in the City of New York*, 2013.

530 6)  J. E. Heffernan and Alex Stephenson. ismev: An Introduction to Statistical Modeling of Extreme Values, *CRAN,* 2012

7)  Dong-Soo Hur, Gyeong-Seon Yeom, Ji-Min Kim, Do-Sam Kim, and Ki-Sung Bae. Estimation of Storm Surges on the Coast of Busan. *Journal of Ocean Engineering and Technology*, 20(3), 37-44, 2006.

8)  Intergovernmental Panel on Climate Change (IPCC). Contribution of working group I to the fourth assessment report of the intergovernmental panel on Climate change. *Cambridge University Press*, 1-996 2007.

535 9)  Yoon-Koo Kang. Patterns of Water Level Increase by Storm Surge and High Waves on Seawall/Quay Wall during Typhoon Maemi. *Journal of Ocean Engineering and Technology*, 19(6), 22-28, 2005.

10) Hyeon-Jeong Kim and Seung-Won Suh. Improved Hypothetical Typhoon Generation Technique for Storm Surge Frequency Analysis on the Southwest Korean Coast. *Journal of Coastal Research, Special Issue*, 85, 516-520, 2018.

11) Tae-Yun Kim and Kwang-Woo Cho. Forecasting of Sea-level Rise using a Semi-Empirical Method. *Journal of the*
540 *Korean Society of Marine Environment and Safety*, 19(1), 1-8, 2013.

12) Korea Hydrographic and Oceanographic Agency. *Korea Real Time Database for NEAR-GOOS*

13) Hyesun Ku, Sungsu Lee, and Yong-Kyu Lee. Statistical model and characteristics of typhoon-induced rainfall around the Korean peninsula. *Journal of the Korean Society of Hazard Mitigation*, 8(5), 45-51, 2008.

14) N. Lin, K. A. Emanuel, J. A. Smith, and E. Vanmarcke. Risk assessment of hurricane storm surge for New York City.
545 *Journal of Geophysical Research*, 115(18), 2010.

15) N. Lin, K. Emanuel, M. Oppenheimer, and E. Vanmarcke. Physically based assessment of hurricane surge threat under climate change. *Nature Climate Change*, 2(6), 462–467, 2012.

16) Madeleine Lopeman, George Deodatis, and Guillermo Franco. Extreme storm surge hazard estimation in lower Manhattan. *Natural Hazards*, 78, 335-391, 2015.

550   17) Madeleine Lopeman. Extreme Storm Surge Hazard Estimation and Windstorm Vulnerability Assessment for Quantitative Risk Analysis. *Ph. D dissertation*, *Columbia University in the City of New York*, 2015.

18) National Typhoon Center. Typhoon technical Book. *Korea Meteorological Administration, National Typhoon Center*, 2011.

19) Noshadravan, T.R. Miller, and J.G. Gregory. A lifecycle cost analysis of residential buildings including natural hazard

555     risk. Journal of Construction Engineering Management, 143, 04017017-1-10, 2017.

20) Valentina Radic and Regine Hock. Regionally differentiated contribution of mountain glaciers and ice caps to future sea-level rise. *Nature Geoscience*, 4, 91-94, 2011.

21) Michiel Schaeffer, William Hare, Stefan Rahmstorf, and Martin Vermeer. Long-term sea-level rise implied by 1.5℃ and 2℃ warming levels. *Nature Climate Change*, 2, 867-870, 2012.

560   22) Alex Stephenson. Harmonic Analysis of Tides, *CRAN*, 2017

23) S. A. Talke, P. Orton, and D. A. Jay. Increasing Storm Tides in New York Harbor, 1844-2013. *Geophysical Research Letters*, 2014.

24) Jong Joo Yoon and Sang Ik Kim. Analysis of Long Period Sea Level Variation on Tidal Station around the Korean Peninsula. *Journal of Coastal Research*, 12(3), 299-305, 2012.

565   25) Chris Zervas. NOAA Technical Report NOS Co-OPS 067: Extreme Water Levels of the United States 1893-2010. *Technical report, National Oceanic and Atmospheric Administration, National Ocean Service, Center for Operational Oceanographic Products and Services*, Silver Spring, MD, 2013.

26) H. Zhong, P. H. A. J. M. van Gelder, P. J. A. T. M. van Overloop, and W. Wang. Application of a fast stochastic storm surge model on estimating the high water level frequency in the Lower Rhine Delta. *Natural Hazards*, 73, 743-759,

570     2014.